IL NUOVO CIMENTO Vol. 34 C, N. 1 Gennaio-Febbraio 2011
DOI 10.1393/ncc/i2011-10820-3

Colloquia: IFA 2010

A Computer-Aided Detection system for lung nodules in CT images

N. Camarlinghi([1])([2]), M. E. Fantacci([1])([2]), I. Gori([3]) and A. Retico([2])

([1]) *Dipartimento di Fisica, Università di Pisa - Pisa, Italy*
([2]) *INFN, Sezione di Pisa - Pisa, Italy*
([3]) *Bracco Imaging S.p.A. - Milano, Italy*

(ricevuto il 9 Luglio 2010; approvato il 26 Luglio 2010; pubblicato online l'1 Marzo 2011)

Summary. — Lung cancer is the leading cause of cancer-related mortality in developed countries. To support radiologists in the identification of early-stage lung cancers, we propose a Computer-Aided Detection (CAD) system, composed by two different procedures: $^{\mathrm{VBNA}}\mathrm{CAD_I}$ devoted to the identification of small nodules embedded in the lung parenchyma (internal nodules) and $^{\mathrm{VBNA}}\mathrm{CAD_{JP}}$ devoted the identification of nodules originating on the pleura surface (juxta-pleural nodules). The CAD system has been developed and tested on a dataset of low-dose and thin-slice CT scans collected in the framework of the first Italian randomized and controlled screening trial (ITALUNG-CT). This work has been carried out in the framework of MAGIC-5 (Medical Application on a Grid Infrastructure Connection), an Italian collaboration funded by Istituto Nazionale di Fisica Nucleare (INFN) and Ministero dell'Università e della Ricerca (MIUR), which aims at developing models and algorithms for a distributed analysis of biomedical images, by making use of the GRID services.

PACS 87.57.-s – Medical imaging.
PACS 87.59.-e – X-ray imaging.
PACS 87.57.Q- – Computed tomography.
PACS 87.57.R- – Computer-aided diagnosis.

1. – Introduction

Lung cancer is the leading cause of cancer-related mortality in developed countries [1, 2]. Only 10–15% of all men and women diagnosed with lung cancer live five years after diagnosis [2, 3] and no significant improvement has occurred in the last 20 years [4]. Early-stage cancer is asymptomatic, so more than 70% of patients diagnosed with lung cancer are in the advanced stages of the disease, when it is too late for effective treatments [5]. However, the five-year survival rate for people diagnosed with early-stage lung cancer (stage I) can reach 70% [6]. In this scenario, the implementation of screening programs for the asymptomatic high-risk population is an approach that is being tried

to reduce the mortality rate of lung cancer. It was proved that screening programs with X-ray radiography do not lead to a reduction in the mortality rate [6-9], due to the low sensitivity of this technique in the identification of small, early-stage cancers. Lung cancer most commonly manifests itself with the formation of non-calcified pulmonary nodules. Computed Tomography (CT) is proved to be the best imaging modality for the detection of small pulmonary nodules, particularly since the introduction of the helical and multi-detector–row technologies [10-12]. Therefore CT-based screening trials are regarded as a promising technique for detecting small, early-stage lung cancers [13, 14]. The ability of low-dose and thin-slice lung CT to make early diagnosis (*i.e.* a stage of the disease in which it is still surgically treatable and curable) has been demonstrated, but one has not demonstrated yet its effectiveness in the actual reduction in the total mortality linked to the disease, probability due to concurrent causes of death in high-risk population. The problem is therefore still open. From a technical point of view, the screening trials have shown that, because of the characteristics of the images to be examined, the effort required of the radiologists is huge, comprising a lot of time for reporting and a high level of specialization in this field. The average number of images for these high-resolution CTs are in fact up to 400, such images are very noisy because of the low dose of radiation required in screening and because of the presence of non-neoplastic abnormalities typical of the high-risk subjects. Moreover, the nodules to be found in the 2D projections are similar to sections of anatomical structures such as airways and blood vessels. It was indeed demonstrated that a large number of nodules (20–35%) risks to be missed in screening diagnoses [15]. In this scenario, Computer-Aided Detection (CAD) methods could be useful to support radiologists in the identification of early-stage pathological objects and the interpretation of diagnostic images is expected to benefit from the advances in computerized image analysis. Although the final diagnosis of medical images is made by the radiologists, they can use the output of a CAD system as a second opinion in detecting lesions and in making diagnostic decision. Despite the fact that a variety of well-established procedures has already been presented to the scientific community, the problem of nodule identification in lung CT is still an open issue. The aim of MAGIC-5 (Medical Application on a Grid Infrastructure Connection), Italian collaboration funded by Istituto Nazionale di Fisica Nucleare (INFN) and Ministero dell'Università e della Ricerca (MIUR), is to develop models and algorithms (see for example [16-20]) for a distributed analysis of biomedical images, by making use of the GRID services. The MAGIC-5 researchers have developed and validated different completely automated CAD methods optimized for the identification of various kinds (in location, dimensions, geometrical shape) of lung nodules in low-dose and thin-slice CT. In this framework we propose the $^{\mathrm{VBNA}}$CAD system, composed by two different procedures: $^{\mathrm{VBNA}}\mathrm{CAD_I}$ devoted to the identification of small nodules embedded in the lung parenchyma (internal nodules, see fig. 1), and $^{\mathrm{VBNA}}\mathrm{CAD_{JP}}$ devoted to the identification of nodules originating on the pleura surface (juxta-pleural nodules, see fig. 2). The $^{\mathrm{VBNA}}$CAD system has been developed and tested on a dataset of low-dose and thin-slice CT scans collected in the framework of the first Italian randomized screening trial (ITALUNG-CT) [21]. The CAD system was implemented in the ITK framework [22], an open-source C++ framework for segmentation and registration of medical images, and the rendering of the obtained results were achieved using VTK [23], a freely available software system for 3D computer graphics, image processing and visualization. The neural networks were implemented using FANN (Fast Artificial Neural Network) [24].

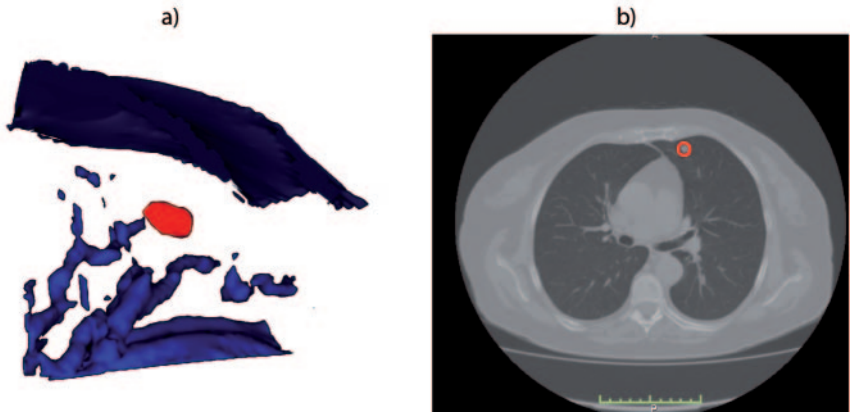

Fig. 1. – (Colour online) Pictures representing an internal nodule. a) Rendering of the internal part of a lung, in red is shown an internal nodule. b) A CT image containing an internal nodule.

2. – The $^{\mathrm{VBNA}}\mathrm{CAD_I}$ system architecture

The strategy we adopted in $^{\mathrm{VBNA}}\mathrm{CAD_I}$ [25, 26] for the automated detection of pulmonary internal nodules is based on the selection of nodule candidates by means of a filter enhancing spherical-shaped objects and on the reduction of the amount of false positive findings by means of a neural classifier developed according to a voxel-based approach [19, 27]. These two main steps of the analysis are applied to appropriate regions of the lung parenchyma, once they have been isotropically resampled and segmented out of the 3D array of CT data by means of a dedicated segmentation algorithm.

2˙1. *Segmentation of the lung parenchyma.* – The aim of the segmentation algorithm implemented in our analysis is to allow a conservative identification of the internal region of the lung parenchyma. In this region we applied the algorithm for internal nodule detection. The 3-dimensional segmentation algorithm, developed according to the procedure proposed in ref. [28], is based on four main steps, as sketched in fig. 3. More in

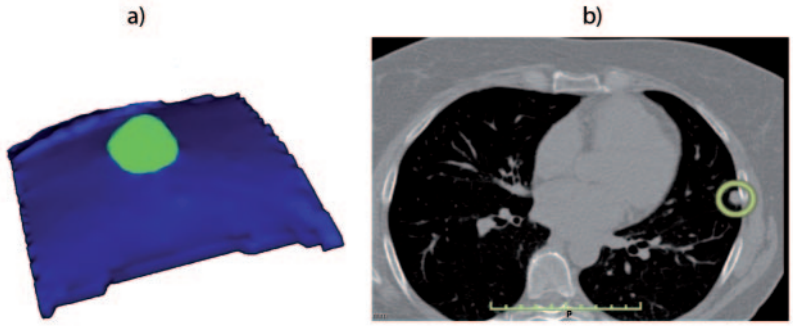

Fig. 2. – (Colour online) Pictures representing a juxta-pleural nodule. a) Rendering of the pleura surface, in green is shown a juxta-pleural nodule. b) A CT image containing a juxta-pleural nodule.

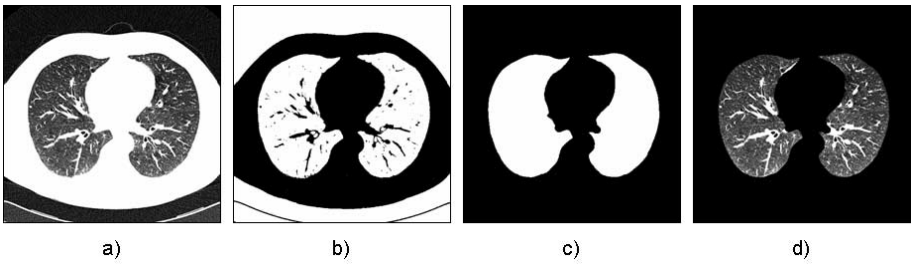

Fig. 3. – Sketch of the 3D segmentation of the lung parenchyma (a slice of the full 3D volume is shown): a) algorithm input (the original CT scan); b) scan appearance after thresholding; c) scan appearance after the selection of connected regions of voxels and morphological operators; d) algorithm output (the segmented lung volume).

details, once the scans have been isotropically resampled, to separate the low-intensity lung parenchyma from the high-intensity surrounding tissue (fat tissue and bones), the voxel intensities are thresholded at a fixed value; then, in order to discard all the regions not belonging to the lungs, the biggest connected component not crossing the boundary of the volume is considered. A rendering of the surface identified by the so-obtained mask is shown in fig. 4, the vessel and airway walls are visible in transparency. Vessels and airways are not in included in the segmented lung at this stage since their volume is outside the segmented lung volume.

To include them without modifying the pleura surface morphology, *i.e.* without modifying the shape of pleura irregularities (including juxta-pleural nodules), a combination of morphological operators is applied. In particular, a sequence of the dilation and the erosion operators with spherical kernels r_d and r_e, with $r_e > r_d$, is implemented. Finally, the logical OR operation between the so-obtained mask and the original lung mask provides the final mask P, where the vessels and the airway walls are filled in, while maintaining the original shape of the lung border.

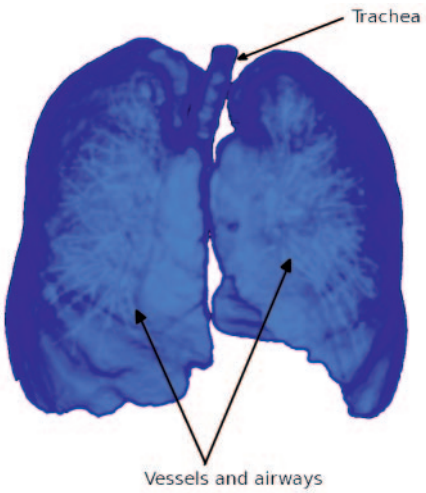

Fig. 4. – Rendering of the surface identified by the mask obtained in the lung segmentation phase before vessels and airway walls filling; the vessels and airway walls are visible in transparency.

2˙2. *Identification of the nodule candidates.* – A very important and difficult task in the automated nodule detection is the selection of nodule candidates. This step of the analysis is required to be characterized by a sensitivity as close as possible to 100%, in order to avoid setting an *a priori* upper bound to the CAD system performance.

To this aim we followed the approach proposed in ref. [29], where nodules are modeled as spherically symmetrical distributions of intensity having a Gaussian profile. A *dot-enhancement* filter has been purposely built to discriminate between these objects and those with elongated and planar shapes. It determines the local geometrical characteristics of each voxel by evaluating the function z_{dot} from the eigenvalues of the Hessian matrix:

$$z_{\mathrm{dot}}(\lambda_1, \lambda_2, \lambda_3) = \begin{cases} |\lambda_3|^2/|\lambda_1|, & \text{if } \lambda_1 < 0,\ \lambda_2 < 0,\ \lambda_3 < 0, \\ 0, & \text{otherwise,} \end{cases}$$

where λ_1, λ_2, λ_3 are the eigenvalues of the Hessian matrix for each voxel, sorted so that $|\lambda_1| > |\lambda_2| > |\lambda_3|$. Signs are appropriate to search for high-intensity objects on a low-intensity background.

To enhance the sensitivity of this filter to nodules of different sizes, a multi-scale approach has to be followed. The filter we used, according to the indications given in ref. [29-31], combines the z_{dot} function with Gaussian smoothing at several scales. This procedure is based on the knowledge of the size of target dataset of nodules: assuming a nodule can be approximated by a 3D Gaussian with scale parameter σ, the nodule diameter can be denoted with 4σ, thus accounting for more than 95% of the nodule volume. If the nodule diameters are in the range $[d_{\min}, d_{\max}]$, the scales to be considered for the Gaussian filter will be in the range $[\sigma_{\min}, \sigma_{\max}]$, where $\sigma_{\min} = s \cdot d_{\min}/4$ and $\sigma_{\max} = s \cdot d_{\max}/4$ and $s = \sqrt{\frac{3}{2}}$ is the normalization factor that was evaluated in ref. [32]. Within that range, the N intermediate smoothing scales are computed as $\sigma_i = r^{i-1}\sigma_{\min}$ where $i = 1, \ldots N$ and $r = (d_{\max}/d_{\min})^{1/(N-1)}$. The resulting filter value is then

$$z_{\max} = \max(\sigma_i^2 z_{\mathrm{dot}}(\sigma_i)) \quad \text{with } i = 1, \ldots N. \tag{1}$$

A peak detection algorithm is then applied to detect local maxima in the filter output matrix. The final output is a list of locations of nodule candidates sorted according to the value of the corresponding $z_{\max}$. In addition to the true nodules, this list is expected to contain also a large number of false positive findings.

2˙3. *False positive reduction.* – To reduce the amount of false positive findings in the list of nodule candidate locations, we developed a procedure we called voxel-based neural approach (VBNA) [33]. First of all, a region of interest (ROI) including the voxels belonging to the candidate nodule is defined according to a simple relative thresholding procedure. Each voxel of a ROI is characterized by the grey level intensity values of its neighborhood. The CT values of the voxel 3D neighborhood are rolled down into a feature vector to be analyzed by a neural classifier (see fig. 5).

The eigenvalues of the gradient and the Hessian matrices computed for each voxel are also encoded to the feature vectors. The gradient matrix is defined as

$$G_{i,j} = \sum \partial_{x_i} I \partial_{x_j} I \quad \text{for} \quad i, j = 1, \ldots 3, \tag{2}$$

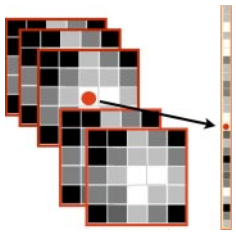

Fig. 5. – Basic idea of the Voxel-Based Neural Approach to false positive reduction: each voxel is characterized by a feature vector constituted by the intensity values of its 3D neighbors and the eigenvalues of the gradient and the Hessian matrices.

where $I(x_1, x_2, x_3)$ is the intensity function (see fig. 5) and the sums are over the neighborhood area, and the Hessian matrix is

$$H_{i,j} = \partial^2_{x_i x_j} I \quad \text{for} \quad i, j = 1, \ldots 3. \tag{3}$$

These six features exploiting the morphology of the voxel neighborhood are added to the textural features given by the intensity values in order to improve the neural-system–discriminating power. A standard three-layered feed-forward neural network is trained at this stage to assign each voxel either to the nodule or to the normal tissue target class. As the final system performance has to be expressed in terms of the trade off between the sensitivity and the number of false positive findings per scan, a procedure to derive the ROI classification from the classification of each single voxel has to be specified: a degree of suspicion is assigned to each ROI evaluating the percentage of voxels tagged as nodule tissue in the ROI.

We can evaluate the entire free-response receiver operating characteristic (FROC) curve for $^{\text{VBNA}}\text{CAD}_{\text{I}}$ system, by varying this threshold [34].

3. – The $^{\text{VBNA}}\text{CAD}_{\text{JP}}$ system architecture

The $^{\text{VBNA}}\text{CAD}_{\text{JP}}$ [25,26] follows a three-step approach: first of all, the pleura surface is identified; then, the candidate nodules are detected by means of a procedure enhancing regions where many pleura surface normals intersect. Finally, a classifier exploiting voxel-based features is implemented to reduce the amount of FP per scan. These three steps are carefully described in the next sections.

3˙1. *Pleura surface identification and representation.* – The pleura surface is defined as the surface identified by the mask P found in sect. **2˙1**. To identify pleural nodules on the surface identified by P is necessary to represent the surface in some way. Representing a surface using cubes (*i.e.* voxels) is an ill-posed problem. To overcome this limit it is common to use an algorithm to transform a binary mask to a polygon mesh [35]. A polygon mesh is a collection of vertices, edges and faces that defines the shape of a polyhedral object in 3D computer graphics and solid modeling. The faces usually consist of triangles, quadrilaterals or other simple polygons. One of the most used algorithm to obtain a mesh from a binary mask is the "marching cube algorithm" [36]. The algorithm proceeds through the scalar field, taking eight neighbor locations at a time (thus forming an imaginary cube), then determining the polygon(s) needed to represent the part of

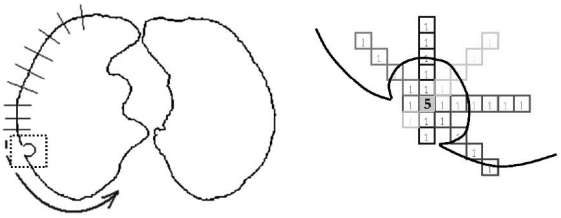

Fig. 6. – Pictures representing the matrix $S(x, y, z)$: each voxel accumulates a score proportional to the number of normals passing through it.

the isosurface that passes through this cube. The individual polygons are then fused into the desired surface. This is done by creating an index to a precalculated array of 256 possible polygon configurations ($2^8 = 256$) within the cube. By means of reflections and symmetrical rotations it is possible to reduce the configurations to 15 unique cases. In this case the marching cube algorithm is applied to the pleura surface found in the previous step. The output of this procedure is a triangular mesh representing the pleura surface.

3˙2. *Candidate nodule selection. – Normal computation:* juxta-pleural nodules can be regarded as concave hemi-spherical objects connected to the pleura surface (see fig. 2). The strategy we adopted to detect them consists in drawing normals to the pleura surface and searching for regions where many normals intersect. Normals are evaluated from the triangular mesh representing the pleura surface. In particular, the normal to each triangle is calculated by using the vector product between the triangle edges; then the normals are evaluated for each vertex by averaging all the normals to the neighbor triangles. This procedure is used in computer graphics to evaluate light reflection on surfaces and it is called "Gouraud shading" [37].

Normal intersection: since the evaluation of the intersections in the real 3D space is a complex and computationally intensive operation, it was implemented in the voxel space. This means that every voxel accumulates a score proportional to the number of normals passing through it. This information is collected in the score matrix $S(x, y, z)$ (see fig. 6). To implement this operation a line rasterization algorithm is needed [38], and the so-called "Bresenhams line algorithm" [39] was chosen. However the intersections in the voxel space are prone to numerical errors and to errors in the computation of the normals, it is preferable to consider Gaussian cylinders instead of line segments. This operation was shown to be equivalent to a Gaussian smoothing of scale $\sigma_{cylinder}$ of the matrix $S(x, y, z)$ [40]

$$A(x,y,z) = \int\int\int S(x',y',z') \frac{\exp\left[-\frac{(x-x')^2+(y-y')^2+(z-z')^2}{2\sigma^2_{cylinder}}\right]}{(\sigma_{cylinder}2\pi)^3} \mathrm{d}x'\mathrm{d}y'\mathrm{d}z'. \tag{4}$$

At the end of this procedure, it is possible to collect the list of locations of nodule candidates looking for the local maxima in the matrix $A(x, y, z)$. Of course, in addition

to the true nodules, this list is expected to contain also a quite large number of false positive findings, mostly due to irregularities in the pleura surface, for example apical scars, pleural thickening, plaques and movement artifacts.

3˙3. *FP reduction.* – A procedure similar to the one described in sect. **2˙3** was implemented. The main difference is that the candidates are segmented using an opening-based procedure instead of a threshold. Each voxel of a ROI is characterized by the grey level intensity values of its neighborhood and the eigenvalues of Hessian and gradient matrix. A standard three-layered feed-forward neural network is trained at this stage to assign each voxel of the 3D array either to the nodule or normal tissue target class. A degree of suspicion is assigned to each ROI evaluating the percentage of voxels tagged as nodule tissue in the ROI. By varying this threshold it is possible to evaluate the FROC curve.

4. – Merging $^{\mathrm{VBNA}}\mathrm{CAD_I}$ and $^{\mathrm{VBNA}}\mathrm{CAD_{JP}}$

At the end of the two CAD procedures it is necessary to merge the findings of $^{\mathrm{VBNA}}\mathrm{CAD_I}$ and $^{\mathrm{VBNA}}\mathrm{CAD_{JP}}$ to obtain the findings for the whole lung. In principle $^{\mathrm{VBNA}}\mathrm{CAD_I}$ and $^{\mathrm{VBNA}}\mathrm{CAD_{JP}}$ should operate on two disconnected regions, *i.e.* the internal part of the lung and the volume outside the pleura surface, but in practice it is possible that the same object is marked by the two CAD procedures. This happens because some pleural nodule can be under-segmented by our procedure. In this case, a part of the nodule is therefore included in the volume of interest of $^{\mathrm{VBNA}}\mathrm{CAD_I}$, giving rise to a double detection by both $^{\mathrm{VBNA}}\mathrm{CAD_I}$ and $^{\mathrm{VBNA}}\mathrm{CAD_{JP}}$. To prevent having two marks pointing the same object, a simple clustering rule was applied: we search for marks with centers closer than 3 mm and, in case of overlapping findings, we delete the finding with the lowest degree of suspicion. This procedure is justified by the fact that overlap happens in particular for nodule objects. In the following part of the manuscript the merged $^{\mathrm{VBNA}}\mathrm{CAD_I}$ and $^{\mathrm{VBNA}}\mathrm{CAD_{JP}}$ procedures will be referred as $^{\mathrm{VBNA}}\mathrm{CAD}$.

5. – Train dataset

The dataset we used to develop, optimize and test the $^{\mathrm{VBNA}}\mathrm{CAD}$ system consists of low-dose and high-resolution CT scans acquired by the Pisa center of the ITALUNG CT trial, the First Italian Randomized Controlled Trial for the screening of lung cancer [21]. The CT scans were acquired with a 4-slice spiral CT scanner according to a low-dose protocol (screening setting: 140 kV, 20 mA), with 1.25 mm slice collimation. The reconstructed slice thickness is 1 mm. The mean number of slices per scan is 300 with a 512×512 pixel matrix, a pixel size ranging from 0.53 to 0.74 mm and 12 bit grey levels in Hounsfield units (HU). The annotations were marked by experienced radiologists, using a dedicated annotation and visualization tool we developed [41]. We considered only non-calcified solid nodules. Some ground-glass opacities had also been selected by radiologists, but their number was too small to allow a dedicated analysis; therefore this type of pathological objects was excluded from our target list.

The training data used for $^{\mathrm{VBNA}}\mathrm{CAD_I}$ consisted of 30 internal nodules contained in 15 CT scans, whereas 28 nodules belonging to 14 CT scans were used for $^{\mathrm{VBNA}}\mathrm{CAD_{JP}}$.

6. – Results on validation datasets

The two presented CAD were validated on three different datasets, using the settings found during the train session.

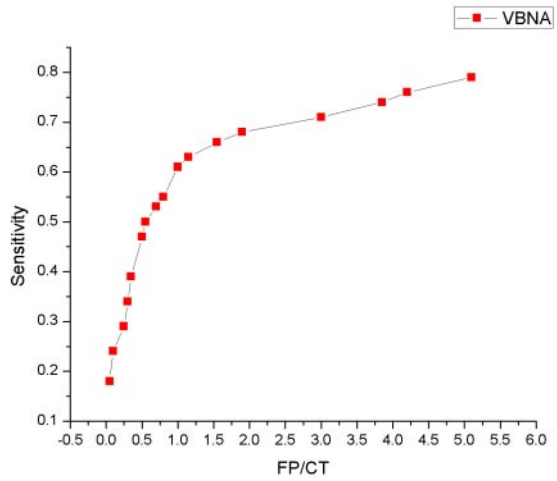

Fig. 7. – FROC curve on a 20 CT dataset of ITALUNG-CT.

6˙1. *ITALUNG-CT*. – The CAD was tested using a dataset of 20 CTs belonging to the ITALUNG-CT screening trial. The 20 CT scans were completely independent of the train dataset. The 20 CTs contained 23 internal nodules and 15 juxta-pleural nodules. Results are shown in terms of the FROC curve in fig. 7.

6˙2. *LIDC*. – The LIDC (Lung Imaging Database Consortium) database is the biggest publicly available collection of annotated CT. LIDC is a multi-center and multi-manufacturer database, currently under development, with cases of different collimation, kVp, tube current and reconstructed slice thickness. At present, about 300 cases of the LIDC database are available, for this study only the 85 available in may 2009 were considered. As shown in fig. 8 only few selected cases have slice thickness comparable to that of ITALUNG-CT database, *i.e.* slice thickness ~ 1 mm. Therefore we expected a drop of performance compared to those obtained on the ITALUNG-CT 20 CT dataset, since, in our opinion, CAD systems are very sensitive to this parameter. The LIDC consortium provides, in order to capture the interreader variability, four different annotations made by four expert radiologists for each case in a two-phase reading modality. The LIDC annotations contain three kinds of objects [42]: nodules with diameters ≥ 3 mm, nodules with diameters < 3 mm and "false positives" with diameters > 3 mm. The contours of the objects marked as nodules with a diameter ≥ 3 mm were provided for every reader together with eight subjective characteristics in a 1–5 scale: subtlety, internal structure, calcification, sphericity, margin, spiculation, texture, malignancy. For nodules with diameters < 3 mm and false positives with diameters < 3 mm only a centroid is provided and no information on the sizes is available. For the evaluation of the $^{\text{VBNA}}$CAD performance, only nodules with diameter ≥ 3 mm were used, since generally very small nodules are typically not considered in screening trial. It is common to report the results on this database using four levels of agreement among the single reader annotations, *i.e.* considering the nodules annotated by at least one, two, three and four radiologists. The correspondence of different findings are not provided in the official LIDC annotations, for this reason we used the correspondences (see table I) and the diameters evaluated in [43].

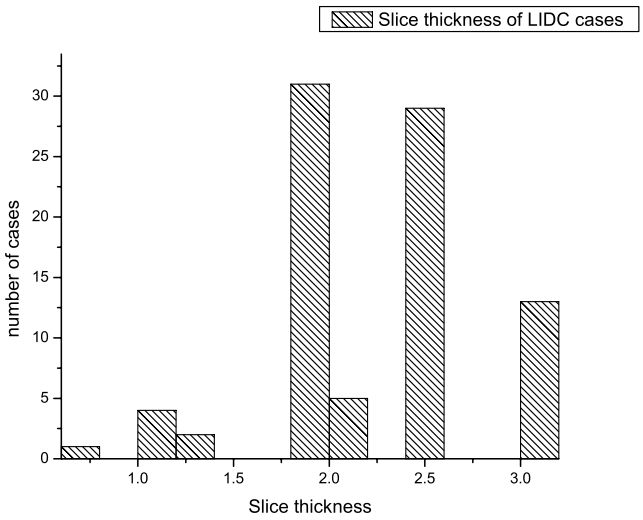

Fig. 8. – Slice thickness of the 85 LIDC cases of this study.

Since the information about the nodule typology, *i.e.* internal nodule or juxta-pleural nodule, was not provided in the LIDC database, it was not possible to evaluate separately the performance of ${}^{\text{VBNA}}\text{CAD}_{\text{I}}$ and ${}^{\text{VBNA}}\text{CAD}_{\text{JP}}$. The results in terms of FROC curves are shown in fig. 9.

6˙3. *ANODE09*. – The ANODE09 [44] is an international initiative devoted to compare objectively different CAD systems able to perform automatic detection of pulmonary nodules in chest CT scans on a single common database, with a single evaluation protocol. Data is provided by the Nelson study, the largest CT lung cancer screening trial in Europe. The images have slice thickness between 0.7 and 1 mm and mean number of slices is 430 per case and were acquired according to a low-dose protocol. Any team, whether from academia or industry, can join this study. The database of this study consists in 5 CT examples with publicly available annotations and 50 low-dose thin-slice CT scans with no public availability of the annotations. The results of the ANODE09 competition and more information on the annotation procedure can be found in ref. [45].

The 50 CTs are intended as a validation dataset, so it is forbidden to use these data as train set for CAD system. The only thing that is public for the 50 CTs is the distribution of nodules diameters: the 40% of nodules are below 4 mm in diameter, the 40% have a diameter between 4 and 6 mm and the 20% is larger. Since annotations

TABLE I. – *Number of nodules with diameters* ≥ 3 mm *for different agreement levels.*

Annotated by at least	Number of nodules with diameter bigger than 3 mm
1 reader	151
2 readers	108
3 readers	77
4 readers	38

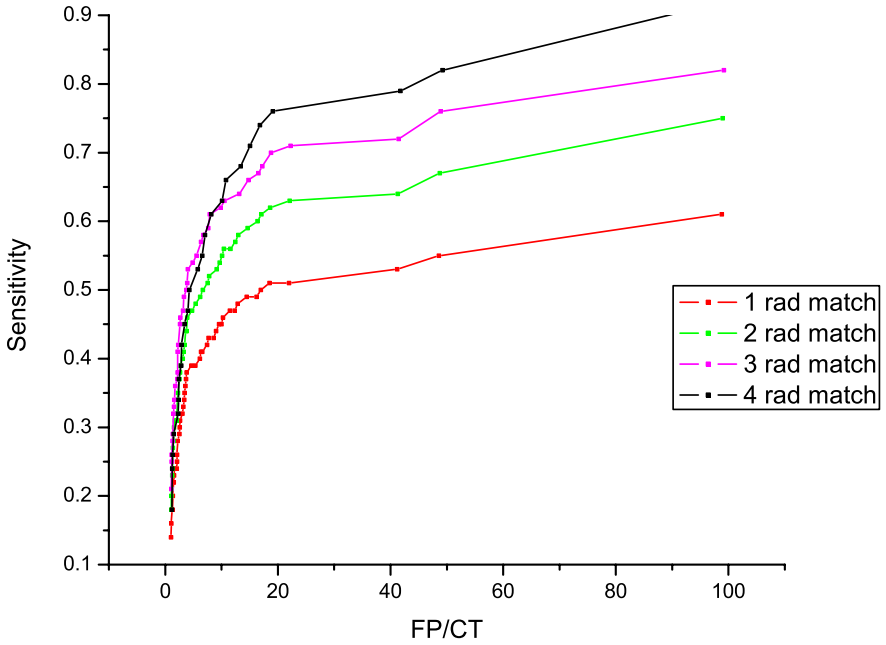

Fig. 9. – FROC for the database LIDC using the four levels (from bottom to top: 1–4) of agreement.

for the 50 CT scans were not publicly available, all the relevant findings should be inserted in a file together with their coordinates and degrees of suspicion, and uploaded on the ANODE09 website [44], to receive in return the FROC curves. The nodules were divided into 7 categories according to their location and shape (see table II). The results, achieved on the 50 CTs for the different kinds of nodules, are shown in terms of mean sensitivity at different FP numbers (1/8, 1/4, 1/2, 1, 2, 4, and 8 FP/CT) in table II and fig. 10. To extract a single score from the FROC curve, the average score on all categories was evaluated. The score of the $^{\text{VBNA}}$CAD was 0.293. The discrepancy between the performance obtained on the 20 CT database (60% sensitivity

TABLE II. – *Summary of the sensitivity obtained in the ANODE09 50 CT study at different FP/CT values.*

FPs/Scan	1/8	1/4	1/2	1	2	4	8	average
small nodules	0.107	0.205	0.299	0.393	0.462	0.564	0.624	0.379
large nodules	0.017	0.022	0.089	0.144	0.222	0.333	0.444	0.182
isolated nodules	0.149	0.214	0.405	0.571	0.571	0.677	0.690	0.467
vascular nodules	0.055	0.116	0.198	0.256	0.372	0.453	0.547	0.285
pleural nodules	0.013	0.034	0.068	0.153	0.220	0.356	0.475	0.188
peri-fissural nodules	0.089	0.171	0.229	0.257	0.286	0.429	0.514	0.282
all nodules	0.068	0.126	0.208	0.285	0.357	0.464	0.546	0.293

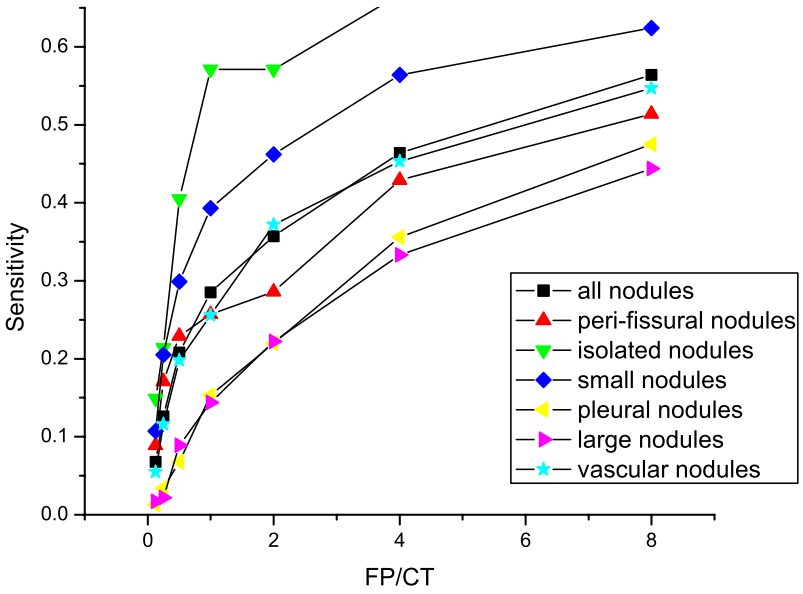

Fig. 10. – FROC curves on the 50 CT ANODE09 dataset, for different nodule typologies. In black is shown the overall curve. Small and big nodules are respectively nodules with diameter $< 5\,\text{mm}$ and $> 5\,\text{mm}$.

at 2.5 FPs/scan on ITALUNG-CT and 43% sensitivity at 2.5 FPs/scan on ANODE09 50 CT) could be explained taking into account the differences between the characteristics of the images of Nelson study and those of ITALUNG-CT.

7. – Conclusions

We proposed a CAD for lung nodules detection in low-dose CT images. The CAD shows the "state of the art" performance on ITALUNG-CT dataset (70% of sensitivity at 3 FP/CT) but shows a decrease of performance if applied on datasets with images acquired according to different protocols. From table II and fig. 10 is also evident that the $^{\text{VBNA}}$CAD works better with isolated nodules and small nodules while its performance is worse for nodules bigger than 5 mm. The decrease of sensitivity was partially expected since big nodules are rarely present in our train dataset. To overcome this limits we plan in the near future to train and validate the whole system on a multi-center and multi-manufacturer database as LIDC [46], using all the available scans. Moreover we plan to validate the $^{\text{VBNA}}$CAD in a clinical trial to assess if the CAD, used as a second reader, is able to help radiologists in reading the images.

* * *

Thanks are due to Dr. A. De Liperi and Dr. F. Falaschi (U.O. Radiodiagnostica 2, Azienda Ospedaliera Universitaria Pisana, Pisa, Italy); Prof. D. Caramella and Dr. M. Barattini (Radiologia Diagnostica e Interventistica, University of Pisa, Italy); Dr. M. Torsello and Dr. I. Zecca (Unità Operativa di Radiologia, Presidio Ospedaliero "V. Fazzi", ASL, Lecce); all the researchers of the MAGIC-5 Collaboration.

REFERENCES

[1] Ferlay J., Autier P., Boniol M., Heanue M., Colombet M. and Boyle P., *Ann. Oncol.*, **18** (2007) 581, PMID: 17287242.

[2] Jemal A., Murray T., Ward E., Samuels A., Tiwari R. C., Ghafoor A., Feuer E. J. and Thun M. J., *CA Cancer J. Clin.*, **55** (2005) 10.

[3] Micheli A., *Ann. Oncol.*, **14** (2003) v28.

[4] Singh G. K., Miller B. A. and Hankey B. F., *J. Nat. Cancer Inst.*, **94** (2002) 916.

[5] Nesbitt J. C., Putnam J. B., Walsh G. L., Roth J. A. and Mountain C. F., *Ann. Thorac. Surg.*, **60** (1995) 466, PMID: 7646126.

[6] Frost J. K., Ball W. C., Levin M. L., Tockman M. S., Baker R. R., Carter D., Eggleston J. C., Erozan Y. S., Gupta P. K. and Khouri N. F., *Am. Rev. Respir. Dis.*, **130** (1984) 549, PMID: 6091505.

[7] Melamed M. R., Flehinger B. J., Zaman M. B., Heelan R. T., Perchick W. A. and Martini N., *Chest*, **86** (1984) 44, PMID: 6734291.

[8] Fontana R. S., Sanderson D. R. and Taylor W. F., *Am. Rev. Respir. Dis.*, **130** (1984) 561.

[9] Marcus P. M., Bergstralh E. J., Fagerstrom R. M., Williams D. E., Fontana R., Taylor W. F. and Prorok P. C., *J. Nat. Cancer Inst.*, **92** (2000) 1308.

[10] Diederich S., Lentschig M. G., Overbeck T. R., Wormanns D. and Heindel W., *Europ. Radiol.*, **11** (2001) 1345, PMID: 11519541.

[11] Kaneko M., Eguchi K., Ohmatsu H., Kakinuma R., Naruke T., Suemasu K. and Moriyama N., *Radiology*, **201** (1996) 798.

[12] Sone S., Takashima S., Li F., Yang Z., Honda T., Maruyama Y., Hasegawa M., Yamanda T., Kubo K., Hanamura K. and Asakura K., *Lancet*, **351** (1998) 1242, PMID: 9643744.

[13] Itoh S., Ikeda M., Arahata S., Kodaira T., Isomura T., Kato T., Yamakawa K., Maruyama K. and Ishigaki T., *Radiology*, **215** (2000) 175.

[14] Henschke C. I., McCauley D. I., Yankelevitz D. F., Naidich D. P., McGuinness G., Miettinen O. S., Libby D. M., Pasmantier M. W., Koizumi J., Altorki N. K. and Smith J. P., *Lancet*, **354** (1999) 99, PMID: 10408484.

[15] Roberts H. C., Patsios D., Kucharczyk M., Paul N. and Roberts T. P., *Int. Cong. Ser.*, **1281** (2005) 1137.

[16] Cerello P., Cheran S. C., Bagnasco S., Bellotti R., Bolanos L., Catanzariti E., De Nunzio G., Fantacci M. E., Fiorina E., Gargano G., Gemme G., Torres E. L., Masala G. L., Peroni C. and Santoro M., *Pattern Recogn.*, **43** (2010) 1476.

[17] Bellotti R., De Carlo F., Gargano G., Tangaro S., Cascio D., Catanzariti E., Cerello P., Cheran S. C., Delogu P., De Mitri I., Fulcheri C., Grosso D., Retico A., Squarcia S., Tommasi E. and Golosio B., *Med. Phys.*, **34** (2007) 4901.

[18] Masala G. L., Tangaro S., Golosio B., Oliva P., Stumbo S., Bellotti R., de Carlo F., Gargano G., Cascio D., Fauci F., Magro R., Raso G., Bottigli U., Chincarini A., de Mitri I., de Nunzio G., Gori I., Retico A., Cerello P., Cheran S. C., Fulcheri C. and Torres E. L., *Nuovo Cimento C*, **30** (2007) 305.

[19] Gori I., Bagagli F., Fantacci M. E., Martinez A. P., Retico A., De Mitri I., Donadio S., Fulcheri C., Gargano G., Magro R., Santoro M. and Stumbo S., *J. Instrum.*, **2** (2007) P09007.

[20] Retico A., Delogu P., Fantacci M. E., Gori I. and Martinez A. P., *Comput. Biol. Med.*, **38** (2008) 525.

[21] Picozzi G., Paci E., Pegna A. L., Bartolucci M., Roselli G., De Francisci A., Gabrielli S., Masi A., Villari N. and Mascalchi M., *Radiol. Med.*, **109** (2005) 17, PMID: 15729183.

[22] See the information available at the web site `http://www.itk.org/`.

[23] See the information available at the web site `http://www.vtk.org/`.

[24] See the information available at the web site `http://leenissen.dk/fann/`.

[25] Gori I., Bagagli F., Camarlinghi N., Fantacci M. E., Retico A., Barattini M., Bolanos L., Falaschi F., Gargano G., Massafra A. and Spinelli C., *Int. J. Comp. Assist. Radiol. Surg.*, **4** Suppl. 1 (2009) S360.
[26] Retico A., Bagagli F., Camarlinghi N., Carpentieri C., Fantacci M. E. and Gori I., "A voxel-based neural approach (VBNA) to identify lung nodules in the ANODE09 study", in *Medical Imaging 2009: Computer-Aided Diagnosis*, *Lake Buena Vista, FL, USA, February 2009*, *Conf. Proc. SPIE*, **7260** (2009) 72601S.
[27] Retico A., Delogu P., Fantacci M. E., Gori I. and Martinez A. P., *Comput. Biol. Med.*, **38** (2008) 525.
[28] Heuberger J., Geissbühler A. and Müller H., *Lung CT segmentation for image retrieval using the Insight Toolkit (ITK)*, *Medical Imaging and Telemedicine (MIT), Wu Yi Mountain, China, August 2005*.
[29] Li Q., Li F. and Doi K., *Acad. Radiol.*, **15** (2008) 165, PMID: 18206615, PMCID: 2266079.
[30] Koenderink J., *Biological Cybernetics*, **50** (1984) 363.
[31] Lindeberg T., *On scale selection for different operators*, in *Proceedings of the Eighth Scandinavian Conference on Image Analysis, Tromso, Norway*, 1993, pp. 857–866.
[32] Sato Y., Nakajima S., Shiraga N., Atsumi H., Yoshida S., Koller T., Gerig G. and Kikinis R., *Med. Image Anal.*, **2** (1998) 143.
[33] Buscema P. M., Patent EP1483721; Gori I. and Mattiuzzi M., Patent EP1880364.
[34] Chakraborty D. P. and Winter L. H., *Radiology*, **174** (1990) 873, PMID: 2305073.
[35] See the information available at the web site `http://en.wikipedia.org/wiki/polygon_mesh`.
[36] Lorensen W. and Cline H., *Marching cubes: A high resolution 3D surface construction algorithm*, in *SIGGRAPH '87: Proceedings of the 14th Annual Conference on Computer Graphics and Interactive Techniques*, Vol. **21** (ACM Press) 1987, pp. 169, 163.
[37] See the information available at the web site `http://it.wikipedia.org/wiki/gouraud_shading`.
[38] See the information available at the web site `http://en.wikipedia.org/wiki/rasterisation`.
[39] See the information available at the web site `http://en.wikipedia.org/wiki/bresenham's_line_algorithm`.
[40] Paik D. S., Beaulieu C. F., Rubin G. D., Acar B., Jeffrey R. B., Yee J., Dey J. and Napel S., *IEEE Trans. Med. Imaging*, **23** (2004) 661, PMID: 15191141.
[41] Gori I., Fantacci M. E., Preite Martinez A. and Retico A., *An automated system for lung nodule detection in low-dose computed tomography*, in *Conf. Proc. SPIE*, **6514** (2007) 65143R1.
[42] See the information available at the web site `https://wiki.nci.nih.gov/display/imaging/lidc`.
[43] See the information available at the web site `https://wiki.nci.nih.gov/display/cip/lidc`.
[44] See the information available at the web site `http://anode09.isi.uu.nl/`.
[45] van Ginneken B., Armato S. G., de Hoop B., van de Vorst S., Duindam T., Niemeijer M., Murphy K., Schilham A. M. R., Retico A., Fantacci M. E., Camarlinghi N., Bagagli F., Gori I., Hara T., Fujita H., Gargano G., Belloti R., De Carlo F., Megna R., Tangaro S., Bolanos L., Cerello P., Cheran S. C., Lopez Torres E. and Prokop M., *Med. Image Anal.*, **14** (2010) 707.
[46] See the information available at the web site `http://imaging.cancer.gov/programsandresources/informationsystems/lidc`.